



1 **Detection of formaldehyde emissions from an industrial zone in the**
2 **Yangtze-River-Delta region of China using a proton transfer reaction**
3 **ion-drift chemical ionization mass spectrometer**

4 Yan Ma^{1,2}, Yiwei Diao^{2,3}, Bingjie Zhang¹, Weiwei Wang³, Xinrong Ren⁴, Dongsen Yang^{1,2,3},
5 Ming Wang¹, Xiaowen Shi^{1,2}, and Jun Zheng^{1,2*}

6 ¹Collaborative Innovation Center of Atmospheric Environment and Equipment Technology,
7 Nanjing University of Information Science & Technology, Nanjing 210044, China

8 ²Yale-NUIST Center on Atmospheric Environment, Nanjing University of Information Science
9 & Technology, Nanjing 210044, China

10 ³Key Laboratory for Aerosol-Cloud-Precipitation of China Meteorological Administration,
11 Department of Atmospheric Physics, Nanjing University of Information Science and Technology,
12 Nanjing 210044, China

13 ⁴Department of Atmospheric and Oceanic Science, University of Maryland, College Park, MD
14 20742, USA

15

16 *Corresponding author:*

17 *Dr. Jun Zheng*

18 *Address: School of Environmental Science and Engineering, Nanjing University of Information*
19 *Science & Technology, Nanjing 210044, China*

20 *Email: zheng.jun@nuist.edu.cn*

21 *Tel.: +86-18251919852*

22 *Fax: +86-25-58731090*

23

24 **Abstract**

25 A proton transfer reaction ion-drift chemical ionization mass spectrometer (PTR-ID-
26 CIMS) equipped with a hydronium (H_3^+O) ion source was developed and deployed near an
27 industrial zone in the Yangtze-River-Delta (YRD) region of China in spring 2015 to investigate
28 industry-related emissions of volatile organic compounds (VOCs). Air pollutants including
29 formaldehyde (HCHO), aromatics, along with other trace gases (O_3 and CO) were simultaneously
30 measured. Humidity effects on the sensitivity of the PTR-ID-CIMS for HCHO detection were
31 investigated and quantified. The performances of the PTR-ID-CIMS were also validated by inter-
32 comparing with off-line HCHO measurement technique using 2,4-dinitrophenylhydrazone
33 (DNPH) cartridges and the results showed fairly good agreement (slope = 0.81, $R^2 = 0.80$). The
34 PTR-ID-CIMS detection limit of HCHO (10-min average) was determined to be 1.7 parts per
35 billion by volume (ppbv) based on three times the standard deviations of the background signals.
36 During the field study, observed HCHO concentration ranged between 1.8 and 12.8 ppbv with a
37 campaign average of 4.1 ± 1.6 ppbv, which was comparable with previous HCHO observations in
38 other similar locations of China. However, HCHO diurnal profiles showed little feature of
39 secondary formation. In addition, time series of both HCHO and aromatic VOCs indicated strong
40 influence from local emissions. Using a multiple linear regression fit model, on average the
41 observed HCHO can be respectively attributed to secondary formation (13.8%), background level
42 (27.0%), and industry-related emissions, i.e., combustion sources (43.2%) and chemical
43 productions (16.0%). Moreover, within the plumes the industry-related emissions can account for
44 up to 69.2% of the observed HCHO. This work has provided direct evidence of strong primary
45 emissions of HCHO from industry-related activities. These primary HCHO sources can
46 potentially have strong impact on local and regional air pollution formation in this area of China.
47 Given the fact that the YRD is the largest economic zone in China and is dense with



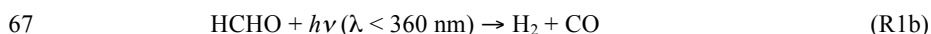
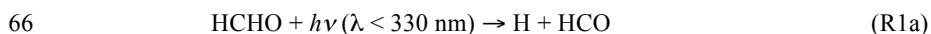
48 petrochemical industries, primary industrial HCHO emissions should be strictly monitored and
49 regulated.

50

51 **Key words:** VOCs; HCHO; CIMS; Ozone; Source Apportionment.

52 **1. Introduction**

53 Formaldehyde (HCHO) has been well recognized as one of the most abundant and
54 important carbonyls in the atmosphere (Dasgupta et al., 2005; Lei et al., 2009; Li et al., 2014;
55 Olaguer et al., 2013; Parrish et al., 2012; Rappengluck et al., 2010). HCHO is ubiquitous in the
56 atmosphere with a typical near-ground concentration ranging from sub-ppbv level in the rural
57 area to ~60 ppbv in highly polluted regions (Finlayson-Pitts and Pitts, 1999). HCHO plays a
58 crucial role in atmospheric photochemistry. The absorption spectrum of HCHO extends well into
59 the UVA region and thus its photolysis rate coefficient (R1) is one of the highest among all
60 carbonyl compounds in the atmosphere (Gratien et al., 2007). Photolysis of HCHO (R1a) can
61 contribute substantially to the atmospheric HO_x radical (OH + HO₂) budget and thus can exert
62 great impact on the oxidative capacity of the atmosphere (Volkamer et al., 2010). Since hydrogen
63 (H₂) is classified as an indirect greenhouse gas, the R1b channel is also of atmospheric
64 importance and may have a non-negligible impact on global climate change (Schultz et al., 2003;
65 Tromp et al., 2003).



68 HCHO is considerably water-soluble. Hence, HCHO may participate in either acid or base
69 catalyzed aldol-condensation reactions in the aerosol phase to contribute to secondary organic
70 aerosol (SOA) formation (Wang et al., 2010). Moreover, HCHO is a known carcinogen. Exposure



71 to HCHO vapor can cause nasal and eye irritation. Breathing in as low as 100 ppbv HCHO may
72 cause allergic reactions in certain population (<http://www.atsdr.cdc.gov/toxfaqs/tfacts111.pdf>).

73 In the background atmosphere, HCHO is mostly formed from photochemical oxidation of
74 methane (CH₄) and terminal alkenes (Finlayson-Pitts and Pitts, 1999). HCHO can also be emitted
75 directly into the air from vegetation although its formation mechanism is not well known (Seco et
76 al., 2007). HCHO flux measurements conducted in forest areas indicate that both plants and the
77 ground surface can contribute to assignable HCHO emissions, although the magnitude of which is
78 relatively small compared to the photochemical production (DiGangi et al., 2011). In contrast to
79 biogenic HCHO sources, anthropogenic activities are often intense primary HCHO sources.
80 HCHO can be produced from any incomplete combustion processes. Vehicle exhaust is believed
81 to be the dominant primary HCHO sources in heavily populated urban areas (Anderson et al.,
82 1996; Ho et al., 2012). Regardless of the types of fuel, all internal combustion engines emit
83 considerable amounts of HCHO. Interestingly, usage of alternative fuels can substantially reduce
84 vehicle emissions of nitrogen oxides (NO_x) but may significantly increase emissions of HCHO
85 and other carbonyl compounds (Wagner and Wyszynski, 1996). Nevertheless, studies have found
86 that vehicle exhaust alone may lead to significant underestimation of the emission inventory of
87 carbonyl compounds in Beijing (Wang et al., 2014), most likely due to the complicated but poorly
88 understood emissions from the industrial sector (Chen et al., 2014). High concentrations of
89 HCHO have been observed around the Houston Ship Channel area populated with petrochemical
90 facilities (Rappengluck et al., 2010). Using an imaging differential optical absorption
91 spectrometer, Pikelnaya et al. (2013) have detected direct HCHO emission from burning flares of
92 the refineries in Houston. In addition to flares, desulfurization and other petrochemical processes
93 such as catalytic cracking of refinery feed may also contribute substantially to primary HCHO
94 emissions (Olaguer et al., 2013). Other industry-related activities, such as wood processing and
95 manufacturing of insect and fungus products also contribute substantial primary HCHO emissions



96 (Garcia et al., 2006). Recent studies have demonstrated that primary carbonyl emissions from a
97 remote oil and gas-production region can lead to high ozone (O₃) formation in a nearby rural area
98 (Edwards et al., 2014). Therefore, it is of practical interest to fully comprehend the detailed
99 primary emission sources of carbonyl compounds, especially in the case of HCHO.

100 Various source apportionment methods have been successfully utilized to identify
101 primary and secondary HCHO sources (Chen et al., 2014; Garcia et al., 2006; Li et al., 2014;
102 Olaguer et al., 2013; Parrish et al., 2012; Zheng et al., 2013b). Due to the lack of carbonyl
103 emission inventories, particularly in China, it is impractical to directly estimate HCHO emissions
104 using emission factors. However, carbon monoxide (CO), sulfur dioxide (SO₂), and toluene have
105 been observed co-emitted with carbonyl compounds from industrial facilities at various locations
106 and hence can serve as tracers of industrial HCHO emission (Pikelnaya et al., 2013; Rappengluck
107 et al., 2010; Wang et al., 2015), i.e., variations of these gases are linearly associated with the
108 primary HCHO emissions. Accordingly, correlation-based methods, such as the multiple linear
109 regression fit model can be used to quantify the relative contribution of primary industrial HCHO
110 sources (Li et al., 2014).

111 HCHO can be measured by various analytical techniques (Gilpin et al., 1997; Li et al.,
112 2005), among which proton transfer reaction mass spectrometry (PTR-MS) does not require
113 sample pretreatments, is free from optical impairment due to heavy aerosol loading, and can
114 potentially achieve a time resolution of a few seconds (Karl et al., 2003). It has been
115 demonstrated that PTR-MS is particularly suitable for capturing strong point sources of VOCs
116 (Zheng et al., 2013a; Zheng et al., 2013b). In this work, a proton transfer reaction ion-drift
117 chemical ionization mass spectrometer (PTR-ID-CIMS) (Fortner et al., 2004; Zheng et al., 2008;
118 Zheng et al., 2010; Zheng et al., 2015a) equipped with a corona discharge hydronium ion source
119 (Zheng et al., 2015b) was developed to investigate VOC-related emissions from an industrial
120 zone in Nanjing, China. The performance of the PTR-ID-CIMS was evaluated by inter-comparing



121 with the more established DNPH (2,4-dinitrophenylhydrazone) technique and the contribution of
122 industry-related activities to primary HCHO emissions was evaluated with a multiple linear
123 regression fit model.

124 **2. Experimental Methods**

125 *2.1 Observation Site*

126 The measurements were carried out from April 15 to 30, 2015 on the campus of the
127 Nanjing University of Information Science & Technology (NUIST). Detailed description of the
128 site has been given in our previous work (Zheng et al., 2015a). Briefly, the site was established by
129 the Chinese Meteorological Administration as a training facility for meteorological observations.
130 Meteorology parameters, including wind direction, wind speed, ambient temperature, pressure,
131 relative humidity, and solar radiation were continuously measured according to Chinese national
132 standards (GB31221-2014). The site was fairly away from local highways and was less than 10
133 km to the west of the heavy industrial zone. When easterly winds were dominant, the site was
134 constantly affected by the outflow from the industry zone (Zheng et al., 2015a). All instruments
135 were housed inside an air-conditioned trailer. The sample line was made of 6.4 mm OD PFA
136 tubing and was installed on the roof of the trailer, about 6 m above the ground level.

137 *2.2 PTR-ID-CIMS*

138 A schematic diagram of the PTR-ID-CIMS is shown in Figure 1. The working principle
139 of the PTR-ID-CIMS is fundamentally the same as a commercial Ionicon PTR-MS (Hansel et al.,
140 1995). The PTR-ID-CIMS consists of a water reservoir, a point-to-surface corona discharge (CD)
141 ion source (Zheng et al., 2015b), a drift tube, and a quadrupole mass spectrometer (Extrel, MAX
142 1000). During operation, 30.0 standard cubic centimeters per minute (SCCM) of ultrapure
143 nitrogen (N₂) regulated by a mass flow controller (Axetris AG) was fed into the water reservoir
144 and then carried water vapor into the CD ion source, where a stainless steel needle biased with



145 ~1300 V discharged on the wall of a 2.5 cm long, 6.4 mm OD stainless steel tubing. Generated
146 hydronium ions (H_3^+O) were pushed into the drift-tube through a 1 mm diameter pinhole. The
147 drift-tube was comprised of eleven 2.5 cm OD, 9.5 mm ID, 6.4 mm thick stainless steel rings that
148 were separated from each other by 1.0 mm thick PTFE spacers. The metal rings were inter-
149 connected with 1.0 M Ω resistors. On the sidewall of the first ring was mounted a PTFE critical
150 orifice limiting the sampling flow to be 340 SCCM. The drift-tube was pumped with an Agilent
151 TS-300 dry scroll pump and the pressure in the drift-tube was 2.0 mbar measured by an Agilent
152 CDG-500 capacitance diaphragm pressure gauge. The voltage between any two adjacent rings
153 was 37.0 V, which produced an electric field of $\sim 52.9 \text{ V cm}^{-1}$. The corresponding ratio of electric
154 field (E) to the buffer gas number density (N), i.e., E/N ratio, was 108 Td (1 Td = $1 \times 10^{-17} \text{ V cm}^2$).
155 To maintain a constant reaction temperature, the drift-tube was regulated at 60 °C. A 200 μm
156 pinhole (Edmund Optics) biased by $\sim 1 \text{ V}$ was used to separate the drift-tube from the high
157 vacuum region that was housing the quadrupole mass analyzer and the Channeltron electron
158 multiplier. The vacuum chamber was differentially pumped by two Agilent TV-301
159 turbomolecular pumps, which shared one Agilent IDP-3 dry scroll pump as the backing pump.
160 Ambient air was delivered to the PTR-ID-CIMS through the 6-m long sample line and a
161 diaphragm pump was used to pump the inlet at ~ 10 standard liters per minute (SLPM) and thus to
162 minimize the sample residence time no more than one second. The inlet was also heated to ~ 60
163 °C to reduce potential wall losses. Using an automatic PTFE 3-way valve, background checks
164 were conducted once every 30 min for 10 min by rerouting sample air through a $\sim 350 \text{ °C}$ Pt
165 catalytic converter (Zheng et al., 2013b; Zheng et al., 2015a).

166 Figure 2 is a typical mass spectrum generated by the PTR-ID-CIMS after scanning the
167 laboratory air by unit mass. Hydronium ion (m/z 19) and its water clusters (m/z 37, m/z 55, m/z
168 73, and m/z 91) can be observed clearly in the spectrum and are the dominant ions. Although
169 oxygen ion (m/z 32) is also present, it is less than 2.5% of the primary hydronium ion (m/z 19)



170 and thus does not interfere significantly with the PTR reactions initiated by hydronium ions.
171 Masses 33, 42, and 59 can be respectively attributed to methanol, acetonitrile, and acetone for the
172 reason that all of these chemicals are commonly utilized as organic solvents in the organic
173 chemistry laboratories in our department. We want to point out that mass 33 can also originate
174 from isotopic peak of O_2^+ with one oxygen-17 ($^{17}OO^+$) and protonated oxygen (HO_2^+), which
175 however are also present during background checks using a catalytic converter and thus both of
176 them will be subtracted from the methanol signal. Mass 59 can also originate from propanal and
177 glyoxal. However, since both propanal and especially glyoxal are significantly more reactive than
178 acetone in the atmosphere, both of them typically contribute less than 10% of the mass 59 signal
179 (de Gouw and Warneke, 2007). The other peaks were most likely due to the chemicals and their
180 fragments originated from various chemistry experiments in the building.

181 In theory, the PTR-ID-CIMS worked essentially in the same way as an Ionicon PTR-MS
182 in VOC detections. However, the PTR-ID-CIMS was developed with an intention to do more
183 than positive ion chemical ionization analysis and thus it was equipped with a bipolar ion
184 detection system. It can be readily converted into a negative ion CIMS. With the proper ion
185 chemistry scheme, the PTR-ID-CIMS can be used to detect not only VOCs but also ammonia
186 (NH_3) (Nowak et al., 2006), nitrous acid (HONO) (Pinto et al., 2014), and nitric acid (HNO_3)
187 (Zheng et al., 2008). In the future, the drift tube can also be modified to adapt an atmospheric
188 pressure interface (API) to do sulfuric acid measurements (Zheng et al., 2010). Another
189 significant difference between the PTR-ID-CIMS and the Ionicon PTR-MS was the inlet system.
190 In the PTR-ID-CIMS air samples were introduced into the drift tube through a critical orifice
191 instead of a long (> 1 m) 1.5 mm OD capillary PEEK tubing used in the Ionicon PTR-MS. We
192 found our inlet setup had the advantages of faster time response and lower wall losses and
193 especially suited for sticky gas measurements, such as NH_3 (Zheng et al., 2015a). In this work,



194 we only want to focus on the measurement and analysis of industry-related VOC emissions by the
195 PTR-ID-CIMS.

196 2.3 HCHO Measurement with PTR-ID-CIMS

197 The PTR-ID-CIMS was operated in the single ion monitor (SIM) mode, i.e., a series of
198 masses were sequentially detected by the PTR-ID-CIMS. The integration time at each mass was
199 set to 2 s and the time interval between two consecutive masses was also set to 2 s. More than 40
200 masses were measured during each measurement cycle and it took about 3 min to finish one cycle.
201 Identification and further analyses of the whole dataset is still an on-going project. HCHO was
202 detected at m/z 31. Because the proton affinity of HCHO is slightly higher than water, reaction
203 R2 is reversible.



205 Therefore, the HCHO measurement using PTR-ID-CIMS was strongly affected by the water
206 concentration in the drift-tube. This water dependency has been investigated in details previously
207 and the sensitivity dependence on water in HCHO detection can be evaluated as the following
208 (Inomata et al., 2008; Jobson and McCoskey, 2010; Schripp et al., 2010; Warneke et al., 2011;
209 Wisthaler et al., 2008; Zheng et al., 2013b):

$$210 \quad [\text{H}^+\text{HCHO}] = \frac{k[\text{HCHO}][\text{H}_3^+\text{O}](1 - e^{-(k[\text{H}_3^+\text{O}] + k'[\text{H}_2\text{O}])t})}{k[\text{H}_3^+\text{O}] + k'[\text{H}_2\text{O}]} \quad (\text{E1})$$

211 where k and k' are the forward and reverse reaction rate coefficients of R2, respectively; t is the
212 ion-molecular reaction time. Given $[\text{H}_2\text{O}] \gg [\text{H}_3^+\text{O}]$, eq. E1 can be simplified and rearranged as
213 eq. E2:

$$214 \quad \frac{[\text{H}^+\text{HCHO}]}{[\text{H}_3^+\text{O}][\text{HCHO}]} = \frac{k(1 - e^{-k[\text{H}_2\text{O}]t})}{k'[\text{H}_2\text{O}]} \quad (\text{E2})$$



215 The left-hand side of the equation indicates that H_3^+O -normalized H^+HCHO counts rate signal
216 (normalized counts per seconds, NCPS) with respect to one ppbv of HCHO (NCPS ppbv^{-1}), or the
217 sensitivity of the PTR-ID-CIMS to HCHO is a function of water vapor concentration inside the
218 drift-tube in the form of (Warneke et al., 2011):

$$219 \quad y = \frac{A}{x}(1 - e^{-Bx}), \quad (\text{E3})$$

220 where x is the water vapor concentration, $A = k/k'$, and $B = k't$. Therefore, the sensitivity of the
221 PTR-ID-CIMS to HCHO at certain humidity can be evaluated according to eq. E2 if the
222 parameters A and B are known. Figure 3 shows a plot of the PTR-ID-CIMS response to HCHO
223 standards under various ambient humidities. Each data point of Fig. 3 was the result of one set of
224 calibration, which will be described in details in the following section. The corresponding water
225 vapor concentration was determined from sample air humidity and the ion source carrier flow
226 humidity. The values of A and B were inferred from curve fitting using eq. E3 as the fitting
227 function. The linear correlation coefficient between the original and fitted values was determined
228 to be 0.82. In addition, given that the reaction temperature and E/N in this work were kept
229 constant (i.e., 60 °C and 108 Td) and the reduced ion mobility of H_3^+O in air was taken as 2.76
230 $\text{cm}^2 \text{V}^{-1} \text{s}^{-1}$ (de Gouw et al., 1997), the ion-molecule reaction time was determined to be about 103
231 μs . Accordingly, k and k' of reaction R2 were also evaluated from A and B with values of $0.84 \times$
232 $10^{-9} \text{cm}^3 \text{molecule}^{-1} \text{s}^{-1}$ and $2.0 \times 10^{-11} \text{cm}^3 \text{molecule}^{-1} \text{s}^{-1}$, respectively. The energy dependency of
233 k and k' has been investigated by Hansel et al. (1997). It was demonstrated that the reverse
234 reaction channel, k' , increased significantly with increasing mean relative kinetic energy (KE) of
235 the reactants while k only showed slightly negative energy dependency. KE under the reaction
236 conditions of this work was calculated according to the method as described by Hansel et al.
237 (1997). The reduced ion mobility of H^+HCHO in air was assumed to be similar as that of
238 $\text{H}_3^+\text{O}\cdot\text{H}_2\text{O}$ ($2.27 \text{cm}^2 \text{V}^{-1} \text{s}^{-1}$) (de Gouw et al., 1997), since they have a similar molecular size.



239 Therefore, the KEs associated with the forward and the reverse reactions were respectively
240 determined to be ~ 0.12 eV and ~ 0.10 eV. The corresponding k and k' measured by Hansel et al
241 (1997) were $\sim 1.4 \times 10^{-9}$ cm³ molecule⁻¹ s⁻¹ and $\sim 1.1 \times 10^{-11}$ cm³ molecule⁻¹ s⁻¹, respectively.
242 Evidently, the inferred values from Fig. 3 agreed fairly well with the literature values.

243 2.4 PTR-ID-CIMS Calibration

244 PTR-ID-CIMS calibrations were performed by mixing gaseous VOC standards (Apel-
245 Reimer Environmental, USA) into zero air through the calibration port. The VOC standard flow
246 rate was controlled by a metal-seal 100 SCCM mass flow controller (UNIT, UFC-1260A). Before
247 each calibration, the PFA tubing to deliver the VOC standard gas was passivated by flowing a
248 few SCCM of VOC standards through it for at least 8 hours. The zero air was normally generated
249 *in situ* by passing ambient air through the catalytic converter and its flow rate was controlled by a
250 critical orifice (as shown in Fig. 1), which was precisely quantified by a Gillibrator (Sensidyne
251 Gilian). Ultra pure nitrogen was also used in place of the zero air to conduct calibrations under
252 the dry condition. The HCHO standard concentration in the cylinder was verified by the DNPH
253 cartridge measurements with a value of 284 ppbv. Background signals were checked before and
254 after the HCHO standard additions using the catalytic converter. The PTR-ID-CIMS was also
255 operated in the SIM mode during calibrations. Similar to the field measurement cycle, the
256 integration time at each mass was set to 2 s and the time interval between two consecutive masses
257 was also set to 2 s. Each calibration cycle contained 48 masses, including m/z 21 ($\text{H}_3^{18}\text{O}^+$), m/z 25
258 (system background), m/z 30 (NO^+), m/z 32 (O_2^+), m/z 37 ($\text{H}_3\text{O}^+\text{H}_2\text{O}$), and other VOC standard
259 gases. It took about 3 minutes to complete one measurement cycle. Figure 4a shows the time
260 series of a typical HCHO calibration. Since the nitrogen-15 isotopic peak of NO ($^{15}\text{NO}^+$) also
261 contributes to the signal at m/z 31, relatively high background signals were observed in Fig. 4a.
262 In addition, because the quadrupole mass filter can normally achieve unit mass separation, m/z 31
263 signals were also slightly interfered by the tail from the relatively strong adjacent oxygen peak



264 (O_2^+), which was about 1 to 2 % of the H_3^+O intensity. Although $^{15}\text{NO}^+$ interference can be
265 removed from the real HCHO signal by background subtraction, to accurately reflect HCHO
266 background signal variations, 0.37% (Hoffmann and Stroobant, 2007) of the signal of m/z 30 (not
267 shown in Fig. 4a) was subtracted from HCHO background check signals before the background
268 noise was evaluated. Each insert in Fig. 4 is the corresponding calibration curve with background
269 signal subtracted. The sensitivity of the PTR-ID-CIMS for HCHO was determined to be 3.1
270 NCPS ppbv^{-1} . For 10-minute average time (3 data points), three times the standard deviation of
271 the background signals was determined to be about 5.3 NCPS and the corresponding HCHO
272 detection limit was estimated to be 1.7 ppbv. The instrument precision was determined by
273 repeated calibrations using pure nitrogen in place of zero air (to avoid the humidity effect). From
274 three consecutive calibrations, we found that the standard deviation of HCHO calibration curve
275 slopes was about 14.5% of the mean value and thus the uncertainty of HCHO measurements were
276 taken as less than 15%.

277 Calibrations of benzene (Fig. 4b) and toluene (Fig. 4c) were conducted using the VOC
278 standard mixture simultaneously with the HCHO calibrations. For 10-minute average time, the
279 calibration factors and detection limits were 41.2 NCPS ppbv^{-1} , 0.06 ppbv for benzene and 40.0
280 NCPS ppbv^{-1} , 0.07 ppbv for toluene, respectively.

281 *2.5 DNPH HCHO Measurements*

282 Carbonyls including HCHO were also measured with the DNPH method followed the US
283 EPA Method TO-11A. Cartridges coated with DNPH (Agela Technologies, Tianjin) were used to
284 scrub carbonyls from the ambient air samples and then analyzed by high-performance liquid
285 chromatography (HPLC) (Waters, Alliance e2695) equipped with a Diamonsil C-18 column
286 ($5\mu\text{m}$, 250 mm by 4.6 mm). The cartridge was attached to the front end of a 6.4 mm OD PFA
287 tubing that was bound to the inlet of the PTR-ID-CIMS. A potassium iodide (KI) cartridge was



288 also installed in the front of the DNPH cartridge to remove ozone. Ambient air was pulled into
289 the cartridges by a diaphragm pump and the flow rate was set to 0.53 SLPM by a critical orifice,
290 which was calibrated with the Gillibrator. The sampling time varied from 0.6 to 2 hours during
291 the campaign depending on the ambient HCHO concentrations. The sampled cartridges were
292 stored in Teflon bags at 4 °C right after sampling.

293 All cartridge samples were processed within two weeks from dates samples were
294 collected. Each sample was first slowly eluted with 5 mL acetonitrile (HPLC grade) and 20.0 µL
295 of the extract solution was injected into the HPLC for analysis. Acetonitrile-water solution (40%
296 to 60%) was used as a gradient mobile phase and the flow rate was set to 1.2 mL min⁻¹. Separated
297 carbonyls were detected by its absorption at 360 nm by a UV detector (Waters 2998). Calibration
298 was conducted with standard solution (Supelco, USA) containing 15 DNPH derivatives of
299 carbonyls, including formaldehyde, acetaldehyde, acrolein, acetone, propionaldehyde,
300 crotonaldehyde, butyraldehyde, benzaldehyde, isovaleraldehyde, valeraldehyde, o-tolualdehyde,
301 m-tolualdehyde, p-tolualdehyde, hexaldehyde, and 2,5-dimethylbenzaldehyde. The dynamic
302 range of a five-point calibration of HCHO spanned from 0.05 to 1.0 µg mL⁻¹ with a linear
303 correlation coefficient of 0.9998. For a two-hour sampling time, the detection limit of HCHO was
304 0.00037 µg mL⁻¹, corresponding to 25 parts per trillion by volume (pptv) at 25 °C, 1.01×10⁵ Pa.
305 The uncertainty of the DNPH method determined from three independent calibrations was less
306 than 3.6%.

307 *2.6 Other Trace Gas Measurements*

308 CO (Thermo Scientific, Model 48i) and O₃ (Thermo Scientific, Model 49i) were also
309 measured at the site. Their operation and calibration procedures followed manufacturer's
310 instructions and have been detailed in previous work (Zheng et al., 2015a).

311 **3. Results and Discussion**

312 *3.1 Overall Observation Results*

313 Meteorological parameters including wind direction, wind speed, relative humidity (RH)
314 and ambient temperature (T) are shown in Fig. 5a and 5b. During the observation period, the
315 weather was mostly clear with occasional precipitation events on April 18, 19, 27 and 28. RH and
316 T showed typical anti-correlation in their diurnal variations. No gusty wind was experienced
317 during the observation period and the average wind speed was $\sim 2.1 \text{ m s}^{-1}$.

318 The time series of O_3 , CO, benzene (C_6H_6), toluene (C_7H_8), and HCHO (10-min-average)
319 are shown in Figure 5c, 5d, and 5e, respectively. Also shown in Fig. 5e (black dots) are the
320 HCHO results from the DNPH cartridge measurements. The gaps in the trace gas measurements
321 were due to either power interruptions or instrument calibrations. High HCHO concentrations up
322 to $\sim 12.8 \text{ ppbv}$ (10-minute averages) were observed in a few pollution episodes. All observed
323 gases showed no obvious diurnal variations, except O_3 , which is a secondary air pollutant mainly
324 formed from photochemical processes (Finlayson-Pitts and Pitts, 1999). Although HCHO was
325 often considered as an intermediate oxidation product of VOCs, such as olefins and CH_4 , we did
326 not observe noticeable diurnal pattern of HCHO in this work either. On the other hand, excellent
327 correlations were found among HCHO, aromatics, and CO, which strongly suggest that primary
328 emissions were responsible for the observed high concentrations of HCHO. In addition, all heavy
329 pollution episodes observed in this campaign were associated with easterly wind or nearly calm
330 weather conditions. For instance, in the afternoon of April 18, the highest concentration of HCHO
331 during the observation period was recorded when the weather was calm with light easterly wind.
332 At $\sim 23:00$, the wind suddenly switched to westerly and the wind speed increased to $2\sim 3 \text{ m s}^{-1}$,
333 bringing in cleaner air masses to the site. HCHO, aromatics, and CO thus decreased sharply to
334 off-peak levels. Clearly, variations in HCHO were highly dependent on wind conditions.



335 The temporal variations of HCHO in this work also differed distinctly from that observed
336 at the Tijuana site during the Cal-Mex 2010 campaign (Zheng et al., 2013b). Although both sites
337 were located in the vicinity of industrial zones, the type of industry in Tijuana was dominated by
338 electronic industries, which normally utilize large quantities of organic solvents (such as
339 methanol, acetone, and ethyl acetate) for electronic parts cleaning during lithography processing
340 (Zheng et al., 2013a). Assisted by the stronger subtropical solar radiation, HCHO in Tijuana was
341 mostly formed from VOC oxidation.

342 *3.2 Inter-comparison with DNPH Cartridge Measurements*

343 The PTR-ID-CIMS HCHO measurements were inter-compared with and verified by the
344 well-established DNPH method. Since the sampling time of the DNPH cartridges was much
345 longer than 10 min, the CIMS data were averaged based on the time stamp for the DNPH
346 cartridge measurements for the inter-comparisons. Overall, both measurements agreed with each
347 other fairly well (Fig. 5e). Figure 6 shows a scatter plot of PTR-ID-CIMS versus DNPH with a
348 slope of 0.81 and an intercept of 0.66 ($R^2 = 0.80$), which can be accounted for by the combined
349 measurement uncertainties and the higher background level in the PTR-ID-CIMS measurements.
350 The reasonably good agreement ensures that the PTR-ID-CIMS could reliably capture relatively
351 high ambient levels of HCHO in this environment.

352 *3.3 Determination of Industrial Emissions*

353 As the observation site is located less than 10 km away from the east of an industrial zone,
354 the site was constantly experiencing plumes originated from various industrial activities, such as
355 crude oil refining, plastic and rubber syntheses, and pesticide productions. Since benzene, toluene,
356 and other aromatics are heavily used in many chemical syntheses, benzene and toluene are mass-
357 produced in the industrial zone by both catalytic cracking of petroleum fractions and coal
358 carbonizations. It is clearly shown in Fig. 5d that toluene and benzene peaks often did not concur



359 simultaneously, indicating that they were emitted from different facilities. Flue gases generated at
360 these facilities were usually incinerated before they were discharged into the atmosphere. In fact
361 many flares could be virtually identified within the industrial zone. Both HCHO and CO were
362 produced during incomplete combustion processes and direct evidence of HCHO emissions from
363 flares have been confirmed by previous observations at oil refineries in Houston, Texas
364 (Pikelnaya et al., 2013). Although it is well known that HCHO and CO were present in vehicle
365 exhaust, the benzene to toluene ratio within CO plumes, as showed in Fig. 5c and 5d, often
366 significantly deviated from 0.5, an indicator of automobile emissions (Hoque et al., 2008),
367 suggesting that these air masses were not dominated by vehicle exhaust. Therefore, HCHO, CO,
368 benzene, and toluene were likely co-emitted from the industrial zone, although they may be
369 originated from different industrial processes and transport-related activities, such as the heavy-
370 duty trucks operating in the vicinity of the industrial zone. Thus both benzene and toluene were
371 selected as tracers of petrochemical industry related sources and CO was selected as the tracer of
372 any combustion processes including flares and vehicle exhaust. Since O₃ was mostly from
373 secondary formation, O₃ was used to represent secondary HCHO. Accordingly, the observed
374 HCHO was apportioned by a multiple linear regression fit model (E4):

$$375 \quad C_{HCHO} = \beta_1 \times C_{O_3} + \beta_2 \times C_{CO} + \beta_3 \times C_{Benzene} + \beta_4 \times C_{Toluene} + \beta_5 \quad (E4)$$

376 where, C_{HCHO} , C_{CO} , $C_{Benzene}$, and $C_{Toluene}$ are measured mixing ratios of HCHO, O₃, CO, benzene
377 and toluene, respectively. β_1 , β_2 , β_3 , β_4 , and β_5 are coefficients obtained from the multiple linear
378 regression fit. β_1 denotes the portion of HCHO from photochemical production. β_2 , β_3 , and β_4 are
379 the emission ratios of HCHO with respect to CO, benzene, and toluene, respectively. β_5
380 represents HCHO concentration in the background atmosphere. According to previous work
381 conducted at a rural site in the YRD region (Wang et al., 2015), the background level of HCHO
382 was constrained to 1.00 ppbv to represent the regional conditions. The multiple linear regression
383 fit analysis was performed with a user-defined fitting function (with the same form as eq. E4)



384 built in the Igor Pro (Version 6.36) software package. The data used for analysis was the same
385 10-minute averaged dataset as the one presented in Fig. 5. The fitting process was initiated by
386 assigning all five parameters ($\beta_1 - \beta_5$) with an initial value of 0.1. After the first run the fitting
387 process was reiterated with the fitting results obtained from the previous run, except that β_5 was
388 constrained to 1 ppbv by default to reflect the regional background conditions. After three
389 iterations, the fitting results did not change from the previous run significantly and the associated
390 standard deviations of the fitted parameters were very close to or less than 0.1. At that point, we
391 considered the fitting results were acceptable.

392 The fitting results are listed in Table 1. The source-apportioned and measured HCHO
393 time series are shown in Fig. 7. In general, the approximated results can capture the trends of
394 measured HCHO profiles fairly well, especially during the pollution episodes. A linear regression
395 fit (Fig. 8) between approximated and measured HCHO shows reasonable agreement with a slope
396 of 0.88 and R^2 of 0.52. The relative contributions of different sources to ambient HCHO are also
397 tabulated in Table 2. Throughout the campaign period, secondary formation accounted for the
398 smallest portion of the observed HCHO regardless within or out of the pollution episodes. The
399 contribution associated with background level of HCHO accounted for about 22% ~ 29% of the
400 total HCHO. CO, benzene, and toluene represented various industry-related activities, such as oil
401 refineries, petrochemical syntheses, power generations, flares, and transportations, which overall
402 contributed substantially (59.2%) to the total HCHO budget and this portion reaches 69.2% when
403 only pollution episodes are considered. The possible reason was that the observation site in this
404 work was in the vicinity of the primary emission sources, which constantly emitted a large
405 quantity of HCHO into the air. These sources were so strong that they can dominate the local
406 photochemical production of HCHO and suppress the typical diurnal variations of HCHO. The
407 good correlations among these otherwise irrelevant air pollutants established a statistical link
408 between HCHO and industrial activities. However, due to the complexity and limited



409 accessibility of the industrial activities, pinpoint the individual emission source of HCHO was
410 virtually impractical in this study. Further detailed investigations within the industrial zone are
411 needed to fully comprehend industrial VOCs emissions.

412 4. Conclusions

413 High concentrations of HCHO were observed using a custom-built PTR-ID-CIMS at a
414 suburban site in Nanjing, China near an industrial zone, typical in the YRD region. The humidity
415 dependency of the PTR-ID-CIMS sensitivity to HCHO was evaluated by systematic calibrations.
416 The PTR-ID-CIMS measurement of HCHO was verified by the US EPA recommended off-line
417 DNPH method (TO-11A). Within the observation period, HCHO ranged between 1.8 and 12.8
418 ppbv with a campaign average of 4.1 ± 1.6 ppbv, which was comparable with previous HCHO
419 observations in other similar locations. Temporal variations of HCHO showed no clear
420 correlation with O_3 , indicating the presence of strong primary point sources of HCHO. All high
421 HCHO episodes observed in this study were associated with air masses originated from the east
422 of the observation site where the industry zone is located and populated with heavy industrial
423 facilities especially petrochemical-related manufacturers. Furthermore, other primary air
424 pollutants including CO, benzene, and toluene were simultaneously measured within the plumes
425 and showed significant correlations with HCHO. Benzene, toluene, and other aromatics were
426 commonly used and mass-produced in petrochemical industries (such as catalytic cracking of
427 petroleum fractions and coal carbonizations) and hence were excellent tracers of petrochemical
428 processes. Both CO and HCHO can be produced during incomplete combustions, such as flares
429 and vehicle exhaust, and thus CO can be considered a tracer of any combustion processes.
430 However, the benzene to toluene ratio was found significantly higher than 0.5 in this work
431 indicating that vehicle exhaust may not be a major contributor to HCHO. Using O_3 , CO, benzene,
432 and toluene as tracers, a multiple linear regression analysis revealed that secondary formation,
433 industry-related activities (flares, various petrochemical productions, and transportation), and the



434 background atmosphere respectively contributed 13.8%, 59.2%, and 27.0% to the observed
435 HCHO. Moreover, within the plumes the portion of industry-related emissions can account for
436 up to 69.2% of the observed HCHO. This work has provided direct evidence of strong primary
437 emissions of HCHO from industry-related activities in China. These primary HCHO sources can
438 potentially have strong impact on local and regional air pollution formation. Given the fact that
439 the YRD region is the largest economic zone in China and is dense with petrochemical industries,
440 primary industrial HCHO emissions should be fully investigated in this area. HCHO emission
441 ratios associated with individual sources are especially needed.

442

443 *Acknowledgements*

444 This work was supported by the National Natural Science Foundation of China (Grant No.
445 41275142, 21377059, and 41575122), Jiangsu Natural Science Foundation (BK2012861), and
446 Jiangsu Provincial Specially-Appointed Professors Foundation.

447 **References:**

- 448 Anderson, L. G., Lanning, J. A., Barrell, R., Miyagishima, J., Jones, R. H., and Wolfe, P.:
449 Sources and sinks of formaldehyde and acetaldehyde: An analysis of Denver's ambient
450 concentration data, *Atmos. Environ.*, 30, 2113-2123, 10.1016/1352-2310(95)00175-1, 1996.
- 451 Chen, W. T., Shao, M., Lu, S. H., Wang, M., Zeng, L. M., Yuan, B., and Liu, Y.: Understanding
452 primary and secondary sources of ambient carbonyl compounds in Beijing using the PMF model,
453 *Atmos. Chem. Phys.*, 14, 3047-3062, 10.5194/acp-14-3047-2014, 2014.
- 454 Dasgupta, P. K., Li, J. Z., Zhang, G. F., Luke, W. T., McClenny, W. A., Stutz, J., and Fried, A.:
455 Summertime ambient formaldehyde in five US metropolitan areas: Nashville, Atlanta, Houston,
456 Philadelphia, and Tampa, *Environ. Sci. Technol.*, 39, 4767-4783, 10.1021/es048327d, 2005.
- 457 de Gouw, J., and Warneke, C.: Measurements of volatile organic compounds in the Earth's
458 atmosphere using proton-transfer-reaction mass spectrometry, *Mass Spectrom. Rev.*, 26, 223-257,
459 2007.
- 460 de Gouw, J. A., Krishnamurthy, M., Bierbaum, V. M., and Leone, S. R.: Measured and calculated
461 mobilities of cluster ions drifting in helium and in nitrogen, *Int. J. Mass spectrom.*, 167, 281-289,
462 1997.
- 463 DiGangi, J. P., Boyle, E. S., Karl, T., Harley, P., Turnipseed, A., Kim, S., Cantrell, C., Maudlin,
464 R. L., Zheng, W., Flocke, F., Hall, S. R., Ullmann, K., Nakashima, Y., Paul, J. B., Wolfe, G. M.,
465 Desai, A. R., Kajii, Y., Guenther, A., and Keutsch, F. N.: First direct measurements of
466 formaldehyde flux via eddy covariance: implications for missing in-canopy formaldehyde sources,
467 *Atmos. Chem. Phys.*, 11, 10565-10578, 10.5194/acp-11-10565-2011, 2011.
- 468 Edwards, P. M., Brown, S. S., Roberts, J. M., Ahmadov, R., Banta, R. M., deGouw, J. A., Dube,
469 W. P., Field, R. A., Flynn, J. H., Gilman, J. B., Graus, M., Helmig, D., Koss, A., Langford, A. O.,
470 Lefer, B. L., Lerner, B. M., Li, R., Li, S.-M., McKeen, S. A., Murphy, S. M., Parrish, D. D., Senff,
471 C. J., Soltis, J., Stutz, J., Sweeney, C., Thompson, C. R., Trainer, M. K., Tsai, C., Veres, P. R.,
472 Washenfelder, R. A., Warneke, C., Wild, R. J., Young, C. J., Yuan, B., and Zamora, R.: High
473 winter ozone pollution from carbonyl photolysis in an oil and gas basin, *Nature*, 514, 351-354,
474 10.1038/nature13767, 2014.
- 475 Finlayson-Pitts, B. J., and Pitts, J. N.: *Chemistry of the upper and lower atmosphere : theory,*
476 *experiments and applications*, Academic Press, San Diego, Calif., xxii, 969 pp., 1999.
- 477 Fortner, E. C., Zhao, J., and Zhang, R. Y.: Development of ion drift-chemical ionization mass
478 spectrometry, *Anal. Chem.*, 76, 5436-5440, doi:10.1021/Ac0493222, 2004.



- 479 Garcia, A. R., Volkamer, R., Molina, L. T., Molina, M. J., Samuelson, J., Mellqvist, J., Galle, B.,
480 Herndon, S. C., and Kolb, C. E.: Separation of emitted and photochemical formaldehyde in
481 Mexico City using a statistical analysis and a new pair of gas-phase tracers, *Atmos. Chem. Phys.*,
482 6, 4545-4557, 2006.
- 483 Gilpin, T., Apel, E., Fried, A., Wert, B., Calvert, J., Zhang, G. F., Dasgupta, P., Harder, J. W.,
484 Heikes, B., Hopkins, B., Westberg, H., Kleindienst, T., Lee, Y. N., Zhou, X. L., Lonneman, W.,
485 and Sewell, S.: Intercomparison of six ambient [CH₂O] measurement techniques, *J. Geophys.*
486 *Res.*, 102, 21161-21188, 10.1029/97jd01314, 1997.
- 487 Gratien, A., Nilsson, E., Doussin, J. F., Johnson, M. S., Nielsen, C. J., Stenstrom, Y., and Picquet-
488 Varrault, B.: UV and IR absorption cross-sections of HCHO, HCDO, and DCDO, *J. Phys. Chem.*
489 *A*, 111, 11506-11513, doi:10.1021/jp074288r, 2007.
- 490 Hansel, A., Jordan, A., Holzinger, R., Prazeller, P., Vogel, W., and Lindinger, W.: Proton-transfer
491 reaction mass-spectrometry - online trace gas-analysis at the ppb level, *Int. J. Mass spectrom.*,
492 149, 609-619, 1995.
- 493 Hansel, A., Singer, W., Wisthaler, A., Schwarzmann, M., and Lindinger, W.: Energy
494 dependencies of the proton transfer reactions $\text{H}_3\text{O}^+ + \text{CH}_2\text{O} \rightleftharpoons \text{CH}_2\text{OH}^+ + \text{H}_2\text{O}^*$, *Int. J. Mass*
495 *spectrom.*, 167, 697-703, doi:10.1016/s0168-1176(97)00128-6, 1997.
- 496 Ho, S. S. H., Ho, K. F., Lee, S. C., Cheng, Y., Yu, J. Z., Lam, K. M., Feng, N. S. Y., and Huang,
497 Y.: Carbonyl emissions from vehicular exhausts sources in Hong Kong, *J. Air Waste Manage.*, 62,
498 221-234, 10.1080/10473289.2011.642952, 2012.
- 499 Hoffmann, E. d., and Stroobant, V.: *Mass Spectrometry - Principles and Applications*, Third
500 Edition ed., John Wiley & Sons, Ltd, 2007.
- 501 Hoque, R. R., Khillare, P. S., Agarwal, T., Shridhar, V., and Balachandran, S.: Spatial and
502 temporal variation of BTEX in the urban atmosphere of Delhi, India, *Sci. Total Environ.*, 392, 30-
503 40, <http://dx.doi.org/10.1016/j.scitotenv.2007.08.036>, 2008.
- 504 Inomata, S., Tanimoto, H., Kameyama, S., Tsunogai, U., Irie, H., Kanaya, Y., and Wang, Z.:
505 Technical Note: Determination of formaldehyde mixing ratios in air with PTR-MS: laboratory
506 experiments and field measurements, *Atmos. Chem. Phys.*, 8, 273-284, 2008.
- 507 Jobson, B. T., and McCoskey, J. K.: Sample drying to improve HCHO measurements by PTR-
508 MS instruments: laboratory and field measurements, *Atmos. Chem. Phys.*, 10, 1821-1835, 2010.
- 509 Karl, T., Jobson, T., Kuster, W. C., Williams, E., Stutz, J., Shetter, R., Hall, S. R., Goldan, P.,
510 Fehsenfeld, F., and Lindinger, W.: Use of proton-transfer-reaction mass spectrometry to



- 511 characterize volatile organic compound sources at the La Porte super site during the Texas Air
512 Quality Study 2000, *J. Geophys. Res.*, 108, 4508, doi:10.1029/2002JD003333, 2003.
- 513 Lei, W., Zavala, M., de Foy, B., Volkamer, R., Molina, M. J., and Molina, L. T.: Impact of
514 primary formaldehyde on air pollution in the Mexico City Metropolitan Area, *Atmos. Chem.*
515 *Phys.*, 9, 2607-2618, 2009.
- 516 Li, J. Z., Dasgupta, P. K., and Luke, W.: Measurement of gaseous and aqueous trace
517 formaldehyde - Revisiting the pentanedione reaction and field applications, *Anal. Chim. Acta.*,
518 531, 51-68, 10.1016/j.aca.2004.09.087, 2005.
- 519 Li, M., Shao, M., Li, L. Y., Lu, S. H., Chen, W. T., and Wang, C.: Quantifying the ambient
520 formaldehyde sources utilizing tracers, *Chin. Chem. Lett.*, 25, 1489-1491,
521 10.1016/j.ccllet.2014.07.001, 2014.
- 522 Nowak, J. B., Huey, L. G., Russell, A. G., Tian, D., Neuman, J. A., Orsini, D., Sjostedt, S. J.,
523 Sullivan, A. P., Tanner, D. J., Weber, R. J., Nenes, A., Edgerton, E., and Fehsenfeld, F. C.:
524 Analysis of urban gas phase ammonia measurements from the 2002 Atlanta Aerosol Nucleation
525 and Real-Time Characterization Experiment (ANARChE), *Journal of Geophysical Research:*
526 *Atmospheres*, 111, D17308, 10.1029/2006JD007113, 2006.
- 527 Olaguer, E. P., Herndon, S. C., Buzcu-Guven, B., Kolb, C. E., Brown, M. J., and Cuclis, A. E.:
528 Attribution of primary formaldehyde and sulfur dioxide at Texas City during
529 SHARP/formaldehyde and olefins from large industrial releases (FLAIR) using an adjoint
530 chemistry transport model, *J. Geophys. Res.*, 118, 11317-11326, 10.1002/jgrd.50794, 2013.
- 531 Parrish, D. D., Ryerson, T. B., Mellqvist, J., Johansson, J., Fried, A., Richter, D., Walega, J. G.,
532 Washenfelder, R. A., de Gouw, J. A., Peischl, J., Aikin, K. C., McKeen, S. A., Frost, G. J.,
533 Fehsenfeld, F. C., and Herndon, S. C.: Primary and secondary sources of formaldehyde in urban
534 atmospheres: Houston Texas region, *Atmos. Chem. Phys.*, 12, 3273-3288, 10.5194/acp-12-3273-
535 2012, 2012.
- 536 Pikelnaya, O., Flynn, J. H., Tsai, C., and Stutz, J.: Imaging DOAS detection of primary
537 formaldehyde and sulfur dioxide emissions from petrochemical flares, *J. Geophys. Res.*, 118,
538 8716-8728, 10.1002/jgrd.50643, 2013.
- 539 Pinto, J. P., Dibb, J., Lee, B. H., Rappenglück, B., Wood, E. C., Levy, M., Zhang, R. Y., Lefer, B.,
540 Ren, X. R., Stutz, J., Tsai, C., Ackermann, L., Golovko, J., Herndon, S. C., Oakes, M., Meng, Q.
541 Y., Munger, J. W., Zahniser, M., and Zheng, J.: Intercomparison of field measurements of nitrous
542 acid (HONO) during the SHARP campaign, *Journal of Geophysical Research: Atmospheres*, 119,
543 2013JD020287, 10.1002/2013JD020287, 2014.



- 544 Rappengluck, B., Dasgupta, P. K., Leuchner, M., Li, Q., and Luke, W.: Formaldehyde and its
545 relation to CO, PAN, and SO(2) in the Houston-Galveston airshed, *Atmos. Chem. Phys.*, 10,
546 2413-2424, 2010.
- 547 Schripp, T., Fauck, C., and Salthammer, T.: Interferences in the determination of formaldehyde
548 via PTR-MS: What do we learn from m/z 31?, *Int. J. Mass spectrom.*, 289, 170-172,
549 10.1016/j.ijms.2009.11.001, 2010.
- 550 Schultz, M. G., Diehl, T., Brasseur, G. P., and Zittel, W.: Air pollution and climate-forcing
551 impacts of a global hydrogen economy, *Science (New York, N.Y.)*, 302,
552 10.1126/science.1089527, 2003.
- 553 Seco, R., Penuelas, J., and Filella, I.: Short-chain oxygenated VOCs: Emission and uptake by
554 plants and atmospheric sources, sinks, and concentrations, *Atmos. Environ.*, 41, 2477-2499,
555 10.1016/j.atmosenv.2006.11.029, 2007.
- 556 Tromp, T. K., Shia, R.-L., Allen, M., Eiler, J. M., and Yung, Y. L.: Potential environmental
557 impact of a hydrogen economy on the stratosphere, *Science (New York, N.Y.)*, 300, 1740-1742,
558 10.1126/science.1085169, 2003.
- 559 Volkamer, R., Sheehy, P., Molina, L. T., and Molina, M. J.: Oxidative capacity of the Mexico
560 City atmosphere - Part 1: A radical source perspective, *Atmos. Chem. Phys.*, 10, 6969-6991,
561 10.5194/acp-10-6969-2010, 2010.
- 562 Wagner, T., and Wyszynski, M. L.: Aldehydes and ketones in engine exhaust emissions - A
563 review, *Proceedings of the Institution of Mechanical Engineers Part D-Journal of Automobile
564 Engineering*, 210, 109-122, 10.1243/pime_proc_1996_210_252_02, 1996.
- 565 Wang, L., Khalizov, A. F., Zheng, J., Xu, W., Ma, Y., Lal, V., and Zhang, R.: Atmospheric
566 nanoparticles formed from heterogeneous reactions of organics, *Nat. Geosci.*, 3, 238-242,
567 doi:10.1038/ngeo778, 2010.
- 568 Wang, M., Shao, M., Chen, W., Yuan, B., Lu, S., Zhang, Q., Zeng, L., and Wang, Q.: A
569 temporally and spatially resolved validation of emission inventories by measurements of ambient
570 volatile organic compounds in Beijing, China, *Atmos. Chem. Phys.*, 14, 5871-5891, 10.5194/acp-
571 14-5871-2014, 2014.
- 572 Wang, M., Chen, W. T., Shao, M., Lu, S. H., Zeng, L. M., and Hu, M.: Investigation of carbonyl
573 compound sources at a rural site in the Yangtze River Delta region of China, *Journal of
574 Environmental Sciences-China*, 28, 128-136, 10.1016/j.jes.2014.12.001, 2015.



- 575 Warneke, C., Veres, P., Holloway, J. S., Stutz, J., Tsai, C., Alvarez, S., Rappenglueck, B.,
576 Fehsenfeld, F. C., Graus, M., Gilman, J. B., and de Gouw, J. A.: Airborne formaldehyde
577 measurements using PTR-MS: calibration, humidity dependence, inter-comparison and initial
578 results, *Atmos. Meas. Tech.*, 4, 2345-2358, 10.5194/amt-4-2345-2011, 2011.
- 579 Wisthaler, A., Apel, E. C., Bossmeyer, J., Hansel, A., Junkermann, W., Koppmann, R., Meier, R.,
580 Muller, K., Solomon, S. J., Steinbrecher, R., Tillmann, R., and Brauers, T.: Technical Note:
581 Intercomparison of formaldehyde measurements at the atmosphere simulation chamber SAPHIR,
582 *Atmos. Chem. Phys.*, 8, 2189-2200, 2008.
- 583 Zheng, J., Zhang, R., Fortner, E. C., Volkamer, R. M., Molina, L., Aiken, A. C., Jimenez, J. L.,
584 Gaeggeler, K., Dommen, J., Dusanter, S., Stevens, P. S., and Tie, X.: Measurements of HNO₃
585 and N₂O₅ using ion drift-chemical ionization mass spectrometry during the MILAGRO/MCMA-
586 2006 campaign, *Atmos. Chem. Phys.*, 8, 6823-6838, 2008.
- 587 Zheng, J., Khalizov, A., Wang, L., and Zhang, R.: Atmospheric pressure-ion drift chemical
588 ionization mass spectrometry for detection of trace gas species, *Anal. Chem.*, 82, 7302-7308,
589 doi:10.1021/ac101253n, 2010.
- 590 Zheng, J., Garzón, J. P., Huertas, M. E., Zhang, R., Levy, M., Ma, Y., Huertas, J. I., Jardón, R. T.,
591 Ruiz, L. G., Tan, H., and Molina, L. T.: Volatile organic compounds in Tijuana during the Cal-
592 Mex 2010 campaign: Measurements and source apportionment, *Atmos. Environ.*, 70, 521-531,
593 <http://dx.doi.org/10.1016/j.atmosenv.2012.11.030>, 2013a.
- 594 Zheng, J., Zhang, R., Garzón, J. P., Huertas, M. E., Levy, M., Ma, Y., Torres-Jardón, R., Ruiz-
595 Suárez, L. G., Russell, L., Takahama, S., Tan, H., Li, G., and Molina, L. T.: Measurements of
596 formaldehyde at the U.S.–Mexico border during the Cal-Mex 2010 air quality study, *Atmos.*
597 *Environ.*, 70, 513-520, <http://dx.doi.org/10.1016/j.atmosenv.2012.09.041>, 2013b.
- 598 Zheng, J., Ma, Y., Chen, M., Zhang, Q., Wang, L., Khalizov, A. F., Yao, L., Wang, Z., Wang, X.,
599 and Chen, L.: Measurement of atmospheric amines and ammonia using the high resolution time-
600 of-flight chemical ionization mass spectrometry, *Atmos. Environ.*, 102, 249-259,
601 <http://dx.doi.org/10.1016/j.atmosenv.2014.12.002>, 2015a.
- 602 Zheng, J., Yang, D., Ma, Y., Chen, M., Cheng, J., Li, S., and Wang, M.: Development of a new
603 corona discharge based ion source for high resolution time-of-flight chemical ionization mass
604 spectrometer to measure gaseous H₂SO₄ and aerosol sulfate, *Atmos. Environ.*, 119, 167-173,
605 <http://dx.doi.org/10.1016/j.atmosenv.2015.08.028>, 2015b.
- 606
- 607



608 **Table 1.** Parameters of the multiple linear regression fit and the linear correlation coefficient (R^2)
609 for the measured and source-apportioned HCHO in Eq. E4. β_1 denotes the portion of HCHO from
610 photochemical production. β_2 , β_3 , and β_4 are the emission ratios of HCHO with respect to CO,
611 benzene, and toluene, respectively. β_5 represents HCHO concentration in the background
612 atmosphere.

β_1 (ppbv/ppbv)	β_2 (ppbv/ppbv)	β_3 (ppbv/ppbv)	β_4 (ppbv/ppbv)	β_5 (ppbv)	R^2
0.0118 ± 0.0012	0.00116 ± 0.000055	0.218 ± 0.014	0.196 ± 0.016	1.00 ± 0.10	0.52

613

614



615 **Table 2.** Relative contributions (%) of different sources to the observed HCHO calculated using
 616 the multiple linear regression model. Pollution episodes are defined as periods when HCHO
 617 concentration was higher than the campaign average, i.e., 4.1 ppbv.

	Secondary (O ₃)	Industry-related emission			Sum of industrial emission	Background
		CO	Benzene	Toluene		
Campaign average	13.8%	43.2%	9.4%	6.6%	59.2%	27.0%
Pollution episodes	8.8%	42.5%	15.1%	11.6%	69.2%	22.0%
Non- pollution period	16.1%	43.6%	6.7%	4.3%	54.6%	29.3%

618

619



620 **Figure Captions:**

621 **Figure 1.** Schematic diagram of the proton transfer reaction ion-drift chemical ionization mass
622 spectrometer (PTR-ID-CIMS).

623 **Figure 2.** A typical mass spectrum produced by the PTR-ID-CIMS in the laboratory.

624 **Figure 3.** The response of the PTR-ID-CIMS to HCHO standards (in the units of counts per
625 second per ppbv HCHO standard per million H_3^+O ion, NCPS ppbv^{-1}) as a function of water
626 vapor concentration inside the drift tube. The correlation is in the form of $y = \frac{A}{x}(1 - e^{-Bx})$,

627 deduced from eq. E1, where A is the ratio between the forward (k) and reverse (k') reaction rate
628 coefficient and B is the product of k' and the ion-molecular reaction time t .

629 **Figure 4.** Time series of a typical set of calibration of HCHO (a), benzene (b), and toluene (c).
630 The insert in each panel is the calibration curve obtained from the corresponding calibration data.

631 **Figure 5.** Time series of meteorological parameters (wind, RH and T) (Panel a and Panel b), trace
632 gases (O_3 and CO) (Panel c), benzene (C_6H_6) and toluene (C_7H_8) (Panel d), and HCHO (Panel e).
633 The black dots in Panel e are DNPH cartridge measurements of HCHO.

634 **Figure 6.** Linear correlation between PTR-ID-CIMS and DNPH measurements of HCHO.

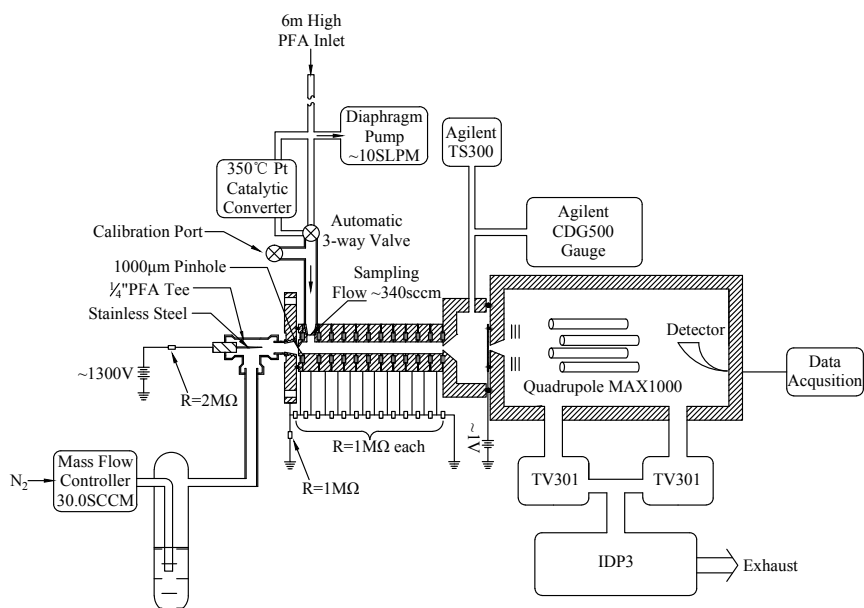
635 **Figure 7.** Comparisons of the measured HCHO and source-apportioned HCHO from the multiple
636 linear regression fit. Measured HCHO is denoted by black dots and contributions from different
637 sources are shown as color coded bars.

638 **Figure 8.** Linear correlation between the approximated and measured HCHO concentrations.
639 Both data sets are synchronized into one-hour temporal resolutions.

640



641



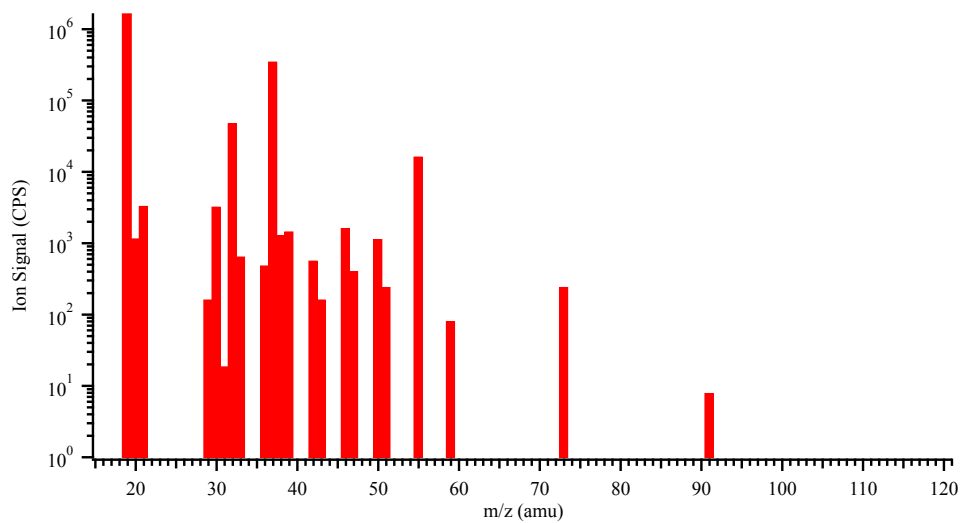
642

643 **Figure 1.** Schematic diagram of the proton transfer reaction ion-drift chemical ionization mass
644 spectrometer (PTR-ID-CIMS).

645



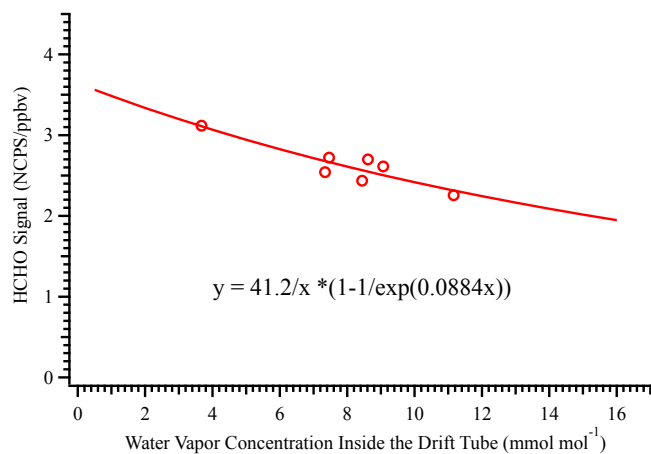
646



647

648 **Figure 2.** A typical mass spectrum produced by the PTR-ID-CIMS in the laboratory.

649



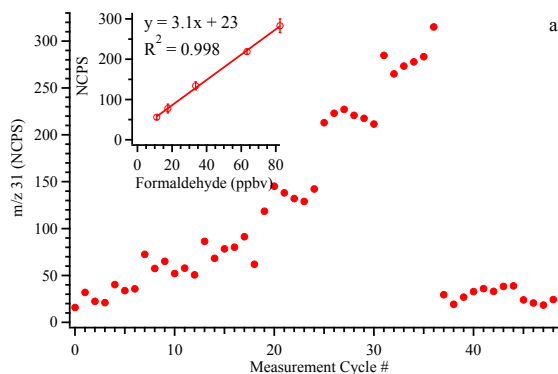
650

651 **Figure 3.** The response of the PTR-ID-CIMS to HCHO standards (in the units of counts per
652 second per ppbv HCHO standard per million H₃⁺O ion, NCPS ppbv⁻¹) as a function of water
653 vapor concentration inside the drift tube. The correlation is in the form of $y = \frac{A}{x}(1 - e^{-Bx})$,
654 deduced from eq. E1, where A is the ratio between the forward (k) and reverse (k') reaction rate
655 coefficient and B is the product of k' and the ion-molecular reaction time t .

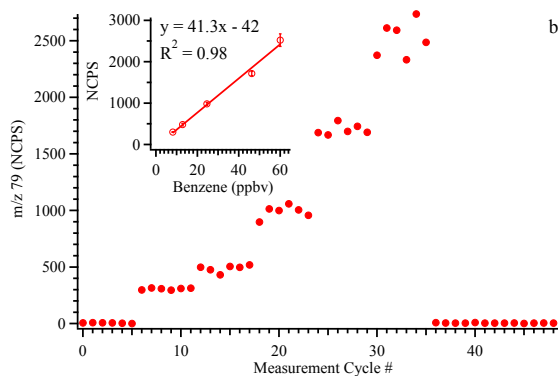
656



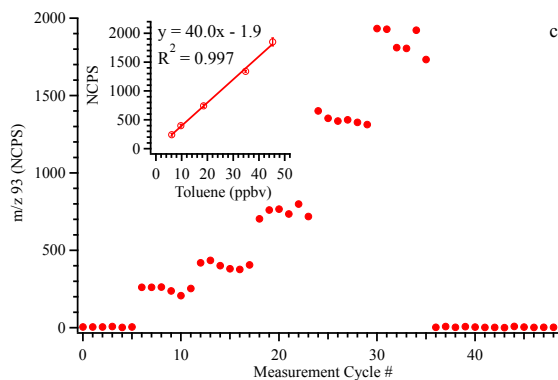
657



658



659



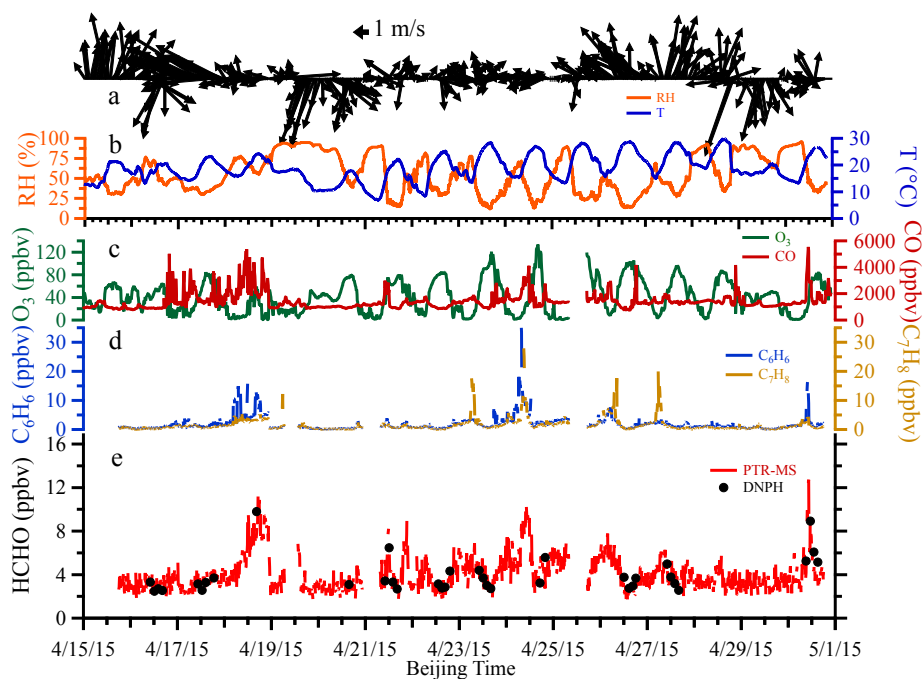
660 **Figure 4.** Time series of a typical set of calibration of HCHO (a), benzene (b), and toluene (c).

661 The insert in each panel is the calibration curve obtained from the corresponding calibration data.

662



663



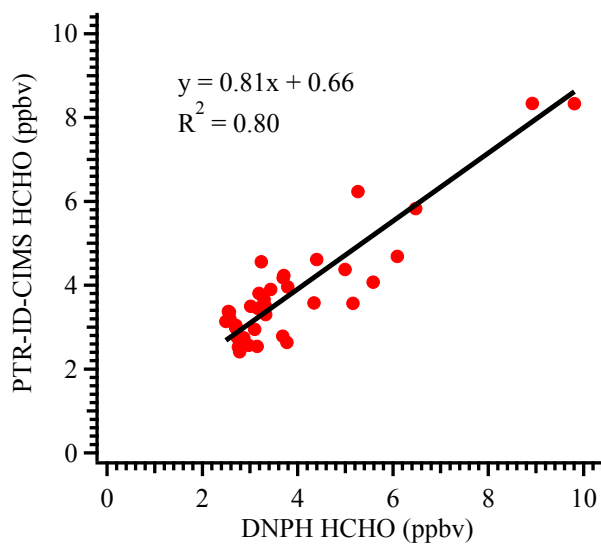
664

665 **Figure 5.** Time series of meteorological parameters (wind, RH and T) (Panel a and Panel b), trace
666 gases (O_3 and CO) (Panel c), benzene (C_6H_6) and toluene (C_7H_8) (Panel d), and HCHO (Panel e).
667 The black dots in Panel e are DNP cartridge measurements of HCHO.

668



669



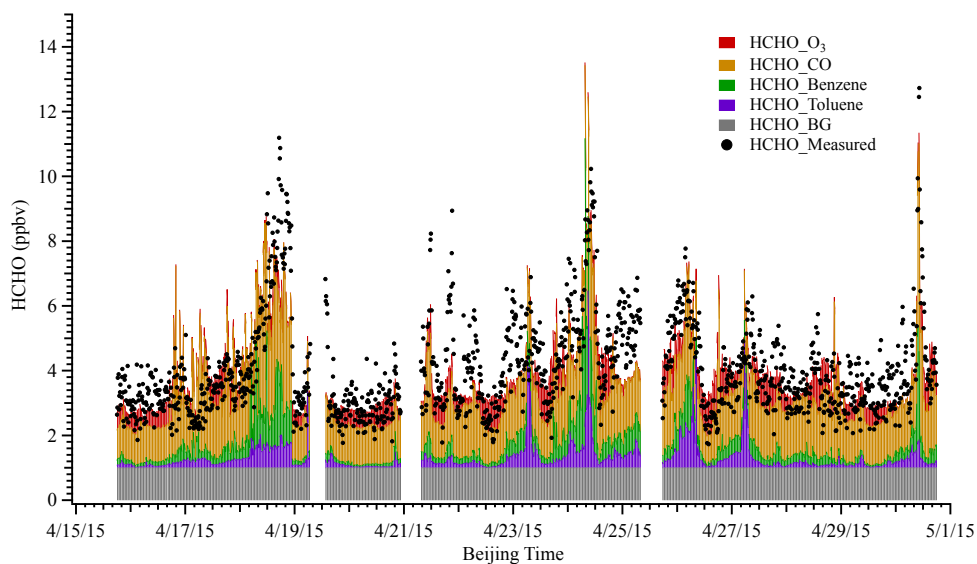
670

671 **Figure 6.** Linear correlation between PTR-ID-CIMS and DNPH measurements of HCHO.

672



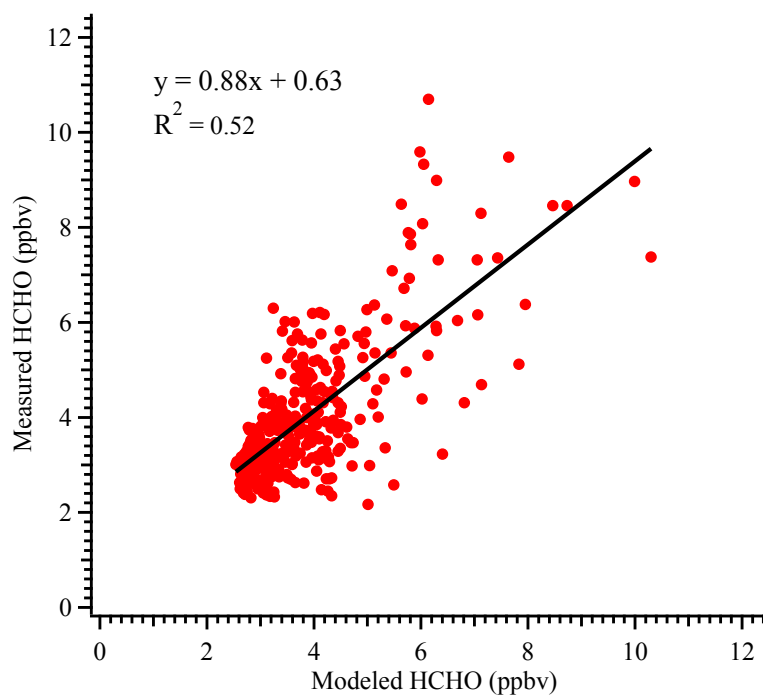
673



674

675 **Figure 7.** Comparisons of the measured HCHO and source-apportioned HCHO from the multiple
676 linear regression fit. Measured HCHO is denoted by black dots and contributions from different
677 sources are shown as color coded bars.

678



679

680 **Figure 8.** Linear correlation between the approximated and measured HCHO concentrations.

681 Both data sets are synchronized into one-hour temporal resolutions.

682